



Study on High-Shear and Low-Pressure Grinding Using Super-Elastic Composite Abrasive Tool (ECAT) for Curved Inconel718 Workpiece

Yebing Tian^{1,2} · Zhiqiang Gu¹ · Sohini Chowdhury¹ · Jinguo Han^{1,2} · Chengwei Wei¹ · Xinyu Fan¹

Received: 1 August 2023 / Revised: 19 April 2024 / Accepted: 25 April 2024
© The Author(s), under exclusive licence to Korean Society for Precision Engineering 2024

Abstract

Inconel718 alloy is widely used in the manufacture of curved parts in aviation and aerospace domain due to its excellent thermal and structural properties. The traditional grinding methods frequently results in low machinability such as grinding burns, surface scratches and clogging in grinding wheel for difficult-to-machine materials. In this work, to eliminate the undesirable outcomes of conventional grinding process, high-shear and low-pressure precision grinding of complex curved Inconel718 workpiece was proposed using specially developed super-elastic composite abrasive tool (ECAT). That was attached to the in-house developed machining system. The influence of composition parameters in various abrasive layers on surface roughness and material removal depth were investigated. The optimal composition parameter of the abrasive layer was determined. The surface morphology, surface profile of the workpiece under different grinding strokes, and grinding force were examined during the high-shear and low-pressure grinding process. The ECAT grinding characteristics were verified at high-shear and low-pressure regime. It was found that the ground surface roughness decreased from initial 306.4 to 50.0 nm after only 8 grinding strokes under the optimal conditions. Also, the surface quality of Inconel718 alloy specimen was significantly enhanced with excellent profile accuracy. It was validated that the high-shear and low-pressure grinding with the developed ECAT was an effective precision machining process for the complex curved parts made of the difficult-to-machine materials.

Keywords Inconel718 alloy · High-shear and low-pressure grinding · Grinding force · Super-elastic composite abrasive tool · Surface roughness · Curved surface

1 Introduction

Inconel718 superalloy has outstanding high temperature properties, thermal fatigue resistance, and good thermal performance even at high temperature and corrosive environments [1–3]. The superalloy is primarily used for fabricating complex curved parts and have wide range of application prospects in the manufacture of key components in aviation and aerospace sector [4, 5]. However, it is often referred as difficult-to-process material due to its typical high-strength

and toughness attribute. Its processing performance is poor and surface quality for cutting-edge items are usually not satisfied.

Grinding is one of the most widely adopted machining processes for difficult-to-machine materials at industrial scale [6, 7]. Traditional grinding wheel is based on multi-edge composite cutting technology. The consolidated abrasive particles on the grinding wheel are employed to cut the surface material in the form of negative rank angles. Furthermore, the grinding forces increase with the increase of the grinding depth of cut [8]. According to the material removal mechanism, the tangential grinding force is a significant factor in the grinding process. In conventional dry grinding of difficult-to-machine materials, the normal component of grinding force is basically 2–3 times larger than the tangential component of grinding force [9]. Small tangential grinding force and large normal grinding force are one of the primary causes of grinding burns, clogging of grinding wheels, poor surface integrity of workpiece

✉ Yebing Tian
tianyeb@sdu.edu.cn; tyb79@sina.com

¹ School of Mechanical Engineering, Shandong University of Technology, 266 Xincun West Road, Zibo 255049, Shandong, People's Republic of China

² Institute for Advanced Manufacturing, Shandong University of Technology, 266 Xincun West Road, Zibo 255049, People's Republic of China

[10, 11]. Hatami et al. [12] developed a cleaning system with a compressed air jet to clean the wheel surface during grinding process of nickel-based superalloy 718. The influences of dry grinding, wet grinding and cleaning systems on surface roughness and grinding ratio were investigated. For the dry grinding condition without cleaning system, the average grinding force ratio F_t/F_n was around 0.39 and the surface roughness was estimated as 587 nm. Lerra et al. [13] developed a finite element model to forecast forces generated by the interaction between a single grain and workpiece material in dry conditions. The model was carried out while varying the cut depth, feed rate and cutting speed. Compared to experiments and simulation, the model predicting the grinding force with an accuracy of about 0.97. There are few researches on grinding force ratio of difficult-to-machine material such as nickel-based superalloys. Grinding of complex curved parts made of nickel-based superalloys is still facing great challenge.

In the recent years, the demand for complex curved parts made of difficult-to-machine material has been increasing. The flexible grinding technology has been widely employed. Traditional belt grinding with good flexibility also provides solution for precision grinding and polishing of various complex curved parts. This method is capable of generating high-quality surface at low cost [14–16]. In addition to the belt grinding, many flexible abrasive tools have emerged. The flexible grinding processes has demonstrated good machining performance for curved workpieces. The abrasive particles employed in the flexible abrasive tools are consolidated in the working layer to achieve flexible grinding. Song and Yao [17, 18] investigated the distribution of pressure with respect to radius of curvature of the airbag and workpiece based on bonnet polishing (BP) and laid the foundation of automatic pressure control. Beaucamp et al. [19] developed a shape adaptive grinding (SAG), which had good processing efficiency and processing quality. Cao et al. [20] proposed a new oscillating precession bonnet polishing method for machining three-dimensional structural surfaces. The polishing process is carried out based on tool path and orientation. Zhu et al. [21] suggested a new polishing technology for blade edge and developed a flexible polishing wheel. This polishing process simultaneously guaranteed the surface roughness and profile accuracy. Compared with the traditional processes, the machining efficiency was greatly improved. Zeng et al. [22] proposed a soft consolidation abrasive (SCA) processing method by consolidating abrasive around the outer periphery of the rubber airbag. The experimental results showed that the SCA had good processing performance on the laser-hardened freeform surface. Wang et al. [23] proposed the freeform generation technique of the slow tool servo with diamond grinding wheel to manufacture free-form optics. A typical of-axis biconical free-form optics with submicron profile accuracy, nanometer surface

roughness, and ductile grinding surfaces was successfully fabricated.

Shear thickening fluid (STF) is a non-Newtonian fluid. When it is subjected to shearing, its scattered particles gather together, referred as the particle cluster effect. Under the action of particle cluster effect, more abrasive particles can be involved in cutting behavior on the workpiece surface. Li et al. [24] polished Si_3N_4 ceramic cylinders using shear thickening fluid. The surface roughness was improved from 107.2 to 6.5 nm after polishing for two hours. Shao et al. [25] proposed the fluid shear thickening polishing (STP) method with the non-Newtonian for effectively polishing nickel-based turbine blades. An efficient and high-quality concave profile was achieved after polishing. Furthermore, the effects of various polishing parameters on the polishing quality was investigated. It was concluded that shear thickening polishing was an effective surface treatment process. Nevertheless, the particle cluster effect is realized by the relative motion of the shear thickening fluid and the workpiece surface. The scratching action on the workpiece surface is weak. The material removal rate is relatively low.

The novel high-shear and low-pressure grinding method with body-armor-like abrasive tool was proposed in our previous work, which was established on the principle of liquid body armor [26–28]. A series of experimental studies were carried out on Inconel 718 alloy specimens to examine the grinding characteristics using the body-armor-like abrasive tool. The high-shear and low-pressure grinding system integrated on the industrial robot was developed [29]. The influence of grinding parameters on grinding quality was investigated for the planar Inconel 718 alloy workpiece. The optimal grinding parameters were obtained. The surface roughness of SLM Inconel718 alloy decreased from 385.2 to 44.5 nm under the optimal parameter condition. The average grinding force ratio of tangential force to normal force was 0.427. The high-shear and low-pressure grinding characteristic of the flexible abrasive tool was verified. It was determined that the improved tangential grinding force enhanced the grinding effect. The simulation of particle clusters were conducted and the effectiveness of high-shear and low-pressure grinding condition at microscopic level was verified [30]. In the previous work, the effects of the grinding parameters such as tool speed, tool offset, and tool feed rate on the surface quality of ground Inconel718 alloys were analyzed. However, the effects of abrasive grain sizes and abrasive mass fractions of the body-armor-like abrasive tool on the surface quality of Inconel 718 alloys has not been explored.

In this work, the high-shear and low-pressure grinding process was developed for curved parts made of Inconel 718 alloys. The super-elastic composite abrasive tool (ECAT) was developed with the principle of liquid body armor. The grinding experiments were carried out on the developed

grinding system for curved Inconel718 alloy. The effect of abrasive layer composition parameters on surface roughness and material removal depth was investigated. The abrasive layer composition parameters were optimized and the optimal abrasive layer composition parameter was determined. The surface morphology and surface contour variation of Inconel718 alloy under different grinding stages were examined.

2 Experimental Details

2.1 Preparation of Abrasive Layer with Super-Elastic Composite Abrasives Tool

The ECAT comprises of upper substrate, hoop, elastic substrate and abrasive layer. The abrasive layer is in direct contact with the workpiece surface to attain material removal. It is the most crucial component in high-shear and low-pressure grinding condition. The grinding quality is significantly influenced by the preparation process of abrasive layer. The upper substrate is 7075 aluminum alloy which is a high strength and light weight material. The elastic substrate is a

Table 1 Parameters of Abrasive layer

Items	Parameters
High-performance fiber	Kevlar29
Abrasive layer based fluid (wt%)	SiO ₂ /PEG system 5, 10, 15
Abrasive (wt%)	Al ₂ O ₃ 5, 7, 9
Average abrasive grain size (μm)	6.5, 10, 13

typical super elastic hemispherical rubber. The diameter of upper substrate and elastomeric substrate are 60 mm each.

The primary elements of abrasive layer are presented in Table 1. The material parameters of Kevlar29 fabric is 1000 D/200 g with a thickness of 2.6 mm is selected due to its excellent performance. The compact warp and weft fibers are woven into Kevlar 29 fabric that provided good dimensional stability and strength retention. Moreover, Kevlar29 fabric exhibited excellent strength, modulus and toughness. Figure 1 shows the abrasive layer preparation flowchart and the ECAT assembly. The first step involves combining hydrophilic fumed nanoscale SiO₂ with PEG200 solution to produce a stable abrasive layer base fluid. It is a non-Newtonian fluid with a shear thickening property. Secondly, Al₂O₃ abrasives and abrasive layer base liquid are combined together to create the abrasive system. Subsequently, the alcohol will be diluted. Thereafter, Kevlar29 is impregnated into the abrasive system. The preparation of abrasive layer is completed after drying [23]. The ECAT is assembled together after the preparation of the abrasive layer.

2.2 Material Removal Mechanism of ECAT

The material removal process of high-shear and low-pressure grinding with the ECAT is shown in Fig. 2. The abrasives and dispersed phases in the abrasive layer are uniformly mixed in the dispersion medium. The composition of the ECAT is illustrated in Fig. 2b. Figure 2c represents that when the high-speed ECAT gets in contact with the workpiece, it collides and crushes the micro-convex peaks on the rough surface of the workpiece. The abrasive particles in the contacted area of the ECAT rapidly generates cluster effect due to the reverse tangential load. When the tangential force exceeds the critical shear yield stress,

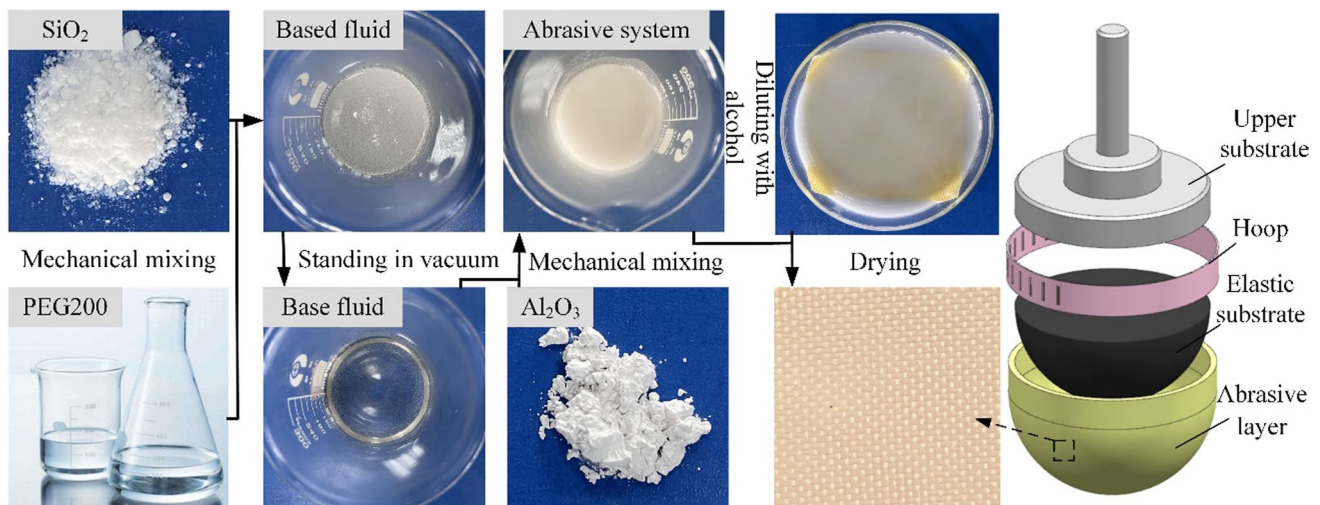


Fig. 1 Flow chart of abrasive layer preparation and configuration of ECAT assembly

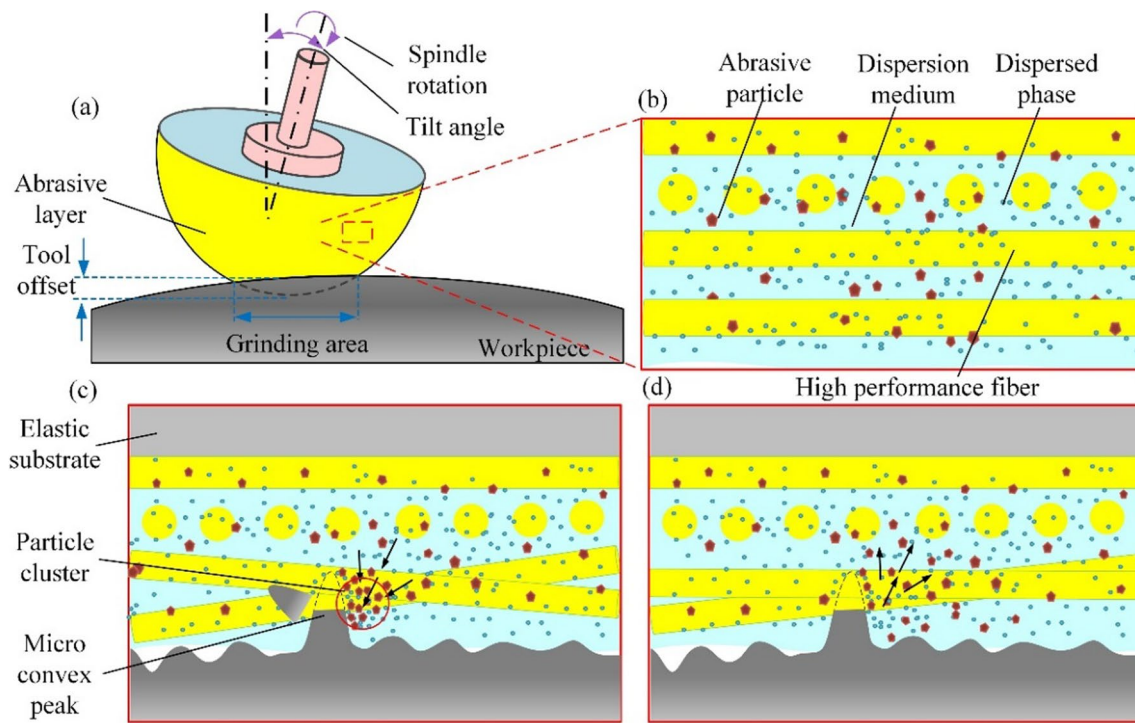


Fig. 2 Material removal mechanism of high-shear and low-pressure grinding with the ECAT

micro-convex peaks on the rough surface of the workpiece are removed with high tangential force and low normal force. After the removal of micro-convex peaks, the particle cluster effects are dispersed. It return to its original state, as shown in Fig. 2d. The high-shear and low-pressure grinding was attained via recycling the removal of the micro-convex peaks on the workpiece surface.

2.3 Experimental Procedure

The high-shear and low-pressure grinding system is presented in Fig. 3. The ECAT is mounted onto the motorized spindle. The Inconel718 workpiece is fixed to the clamping vice. It is tightened on the dynamometer on the precision worktable.

The experimental conditions are shown in Table 2. The curved Inconel718 workpiece has a length of 60 mm, width

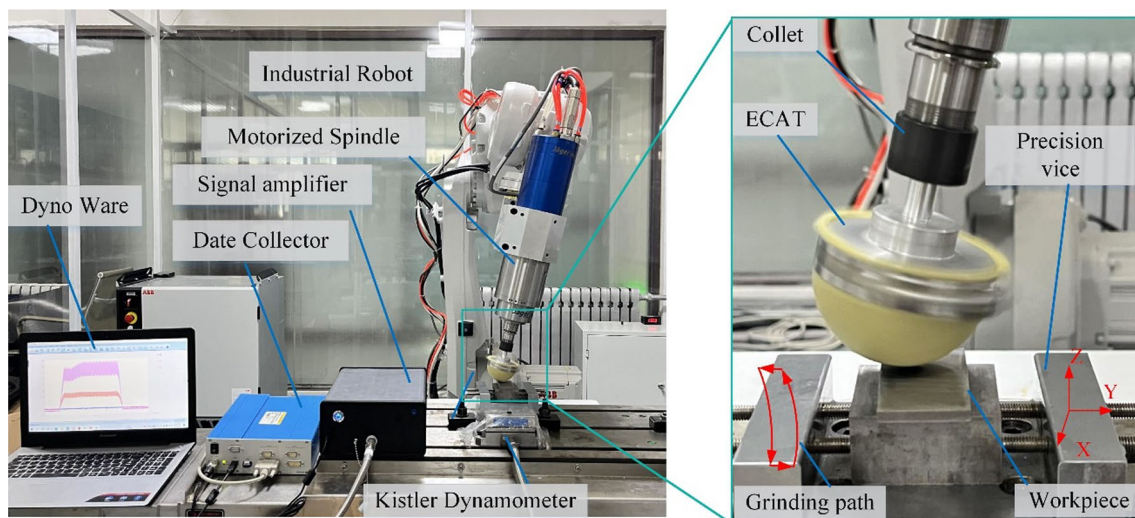


Fig. 3 High-shear and low-pressure grinding system

Table 2 Grinding parameters

Items	Parameters
Tool offset (mm)	1
Tool feed rate (mm/s)	4
Tool speed (r/min)	600
Tilt angle (°)	15
Total number of strokes	8
Workpiece material	Inconel718
Tool path motion	Circular path

of 30 mm, height of 8 mm and a surface radius of 151.5 mm. RobotStudio 6.08, an offline programming software for ABB robot, is used for programming the trajectory motion and simulation. The grinding path is set to a circular path such that it fits the curved surface. As shown in Fig. 3, the ECAT is fitted to the curved workpiece along the +x axis for circular motion and the feed movement is carried out along the +y axis direction. The grinding depth of cut is 0.6 mm. It goes around the -x axis and subsequently it comes back to the starting point. The movement of grinding stroke is completed and the total grinding stroke is 8. The grinding parameters are set to tool offset of 1.0 mm, tool feed speed of 4 mm/s and tool speed of 600 r/min. The optimal combination of grinding parameters was adopted according to the previous investigation [29–31].

2.4 Characterization

A portable roughness measuring instrument (Model: Time3200) was employed to measure the surface irregularities at five distinct locations in the grinded area. The surface roughness was determined by considering an average result of five measurements. The assessment length was 4.0 mm and the sampling length for the measurement was 0.8 mm.

For characterizing the surface topography of the specimen DSX1000 digital microscope (OLYMPUS) was employed. The SEM topography of the sample was recognized using a field emission scanning electron microscope (Quanta 250). The UP-Lambda profilometer (Rtec) was used to assess the three-dimensional topography and surface profile of the ground workpiece. During each surface inspection, the workpiece was fixed at the same position of the stage. In addition, the surface profile were measured at the same workpiece position under different grinding strokes.

The grinding force was measured with the piezoelectric system (Kistler 9257B). The grinding mode was fixed point grinding and the sampling frequency was set at 2000 Hz. The grinding area was the top surface and the grinding duration was 5 s. The acquired grinding force signals were drifted and low-pass filtered. The filter frequency was set at 15 Hz. The force ratio was the average force ratio at stable grinding stages.

3 Results and Discussions

At high-shear and low-pressure grinding condition, the abrasive layer was the most important element of ECAT that directly contacted with the specimen surface to achieve material removal. The preparation of the abrasive system determined the shear thickening characteristics of the abrasive layer. It also had an important influence on the grinding performance of the ECAT.

3.1 Surface Morphology of the Abrasive Layer

Initially, the microscopic surface morphology of the pure fiber as well as the abrasive layer is identified. Figure 4a shows the SEM images of pure fibers. It is recognized that the pure fibers are compactly arranged and the surface of the fiber filament is smooth. Figure 4b illustrates the SEM

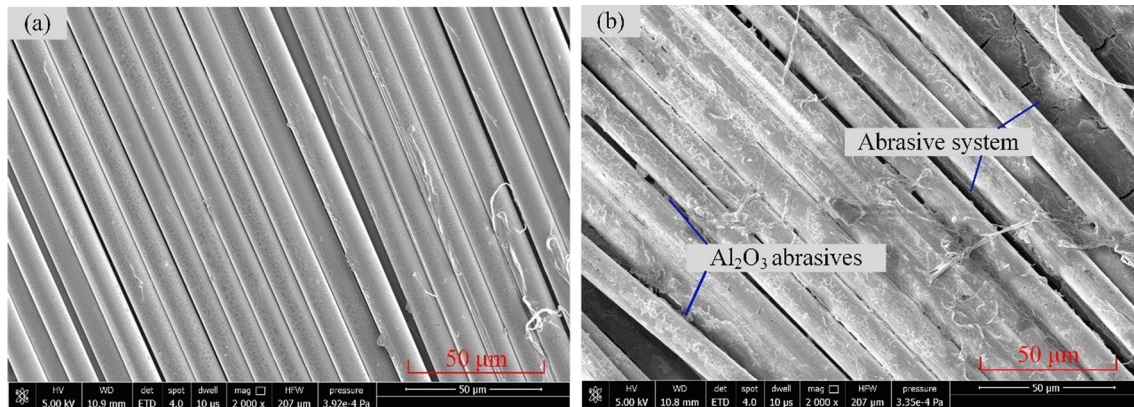


Fig. 4 Microscopic surface morphology of **a** pure fiber and **b** abrasive layer

images of abrasive layer and it is determined that the abrasive system contains large proportion of alumina grains which are attached to the surface of the fiber filaments. The surface morphology demonstrates that the abrasive layer is prepared in good condition.

3.2 Surface Roughness

3.2.1 Influences of Abrasive Layer Base Fluid Mass Fractions on Surface Roughness

The surface roughness of Inconel718 specimen was examined at different mass fractions of abrasive layer base fluid with the fixed abrasive grain size of $6.5\ \mu\text{m}$ and Al_2O_3 abrasive mass fractions of 5% (refer Fig. 5). The best grinding quality was obtained as the mass fraction of abrasive layer base fluid was 15%. The surface roughness (R_a) reduced from 306.4 to 50.0 nm with the improvement of about 83.6%. The worst grinding quality was obtained at 5% mass fractions of abrasive layer base fluid. This contributed to the fact that the lower the nano silica mass fraction worsened the shear thickening properties of the abrasive layer base liquid. The mass fraction of fluid in the abrasive layer represented the mass fraction of SiO_2 nanoparticles in the base fluid. The decrease of the mass fraction of SiO_2 worsened the shear-thickening properties of the abrasive layer-based fluid. It was determined that the shear-thickening properties of the abrasive layer-based fluids were significantly weakened for mass fractions of 5% and 10% during the preparation of the base fluid. The increase of the mass fraction of nano- SiO_2 in the abrasive layer-based fluid per unit mass, it is more likely for the fluid to form shear-thickening effect. Therefore, the fluid-based abrasive layer containing 15% mass fraction of nano- SiO_2 was most effective.

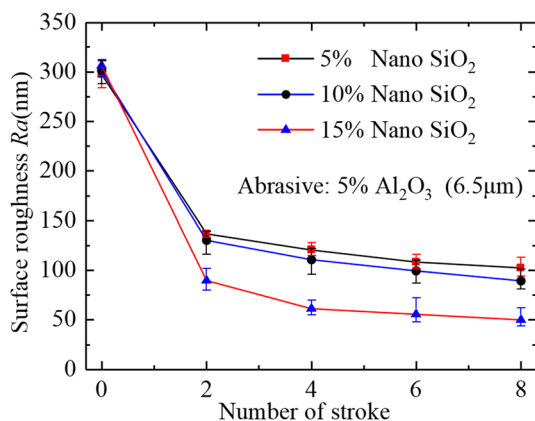


Fig. 5 Surface roughness variations versus grinding strokes at different abrasive layer base fluid mass fractions

3.2.2 Influences of Average Abrasive Grain Size on Surface Roughness

Figure 6 shows the variation of the surface roughness versus grinding strokes at different abrasive grain sizes. The abrasive mass fraction and the mass fraction of abrasive layer base liquid was fixed at 5% and 15%, respectively. When the particle size of Al_2O_3 abrasive was $6.5\ \mu\text{m}$, $10\ \mu\text{m}$ and $13\ \mu\text{m}$, the final surface roughnesses after 8 grinding strokes were 50.0 nm, 62.1 nm and 79.2 nm, respectively. It was found that the surface roughness increased with the increase of the abrasive particle size. The best surface roughness was achieved at the abrasive grain size of $6.5\ \mu\text{m}$. The surface roughness decreased rapidly in the first 2 grinding strokes while it varied slightly after 2–4 grinding strokes. The shear-thickening effect occurred on the asperities of the workpiece surface during high-shear and low-pressure grinding. The large micro-convex peaks on the workpiece surface i.e. rough surface and small grain size are relatively easy to generate cluster effects. The asperities were easy to be removed. After 2–4 grinding strokes, the workpiece surface rapidly became ultra-smooth. The surface roughness varied slowly as the shear-thickening effect weakened.

3.2.3 Influences of Abrasive Mass Fraction on Surface Roughness

Figure 7 shows the variation of surface roughness versus grinding strokes at different abrasive mass fractions. The mass fraction of abrasive layer base fluid was chosen as 15%. The abrasive grain size was fixed at $6.5\ \mu\text{m}$. The surface roughness (R_a) was obtained as 111.6 nm, 95.2 nm, and 50.0 nm after 8 grinding strokes at the abrasive mass fraction of 9%, 7%, and 5%, respectively. The surface roughness was lowest at the abrasive mass fraction of 5% while it was largest at abrasive mass fraction of 9%. Figure 8 exhibits

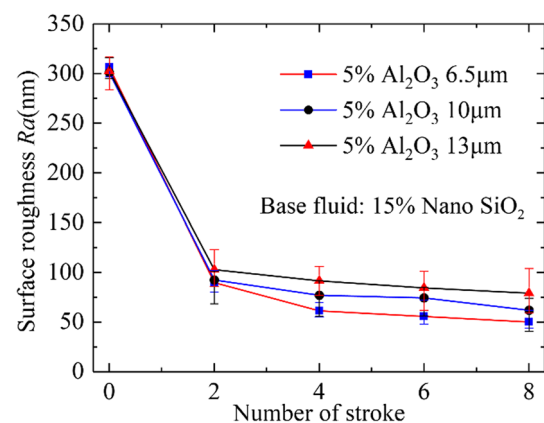


Fig. 6 Surface roughness variations versus grinding strokes at different abrasive grain sizes

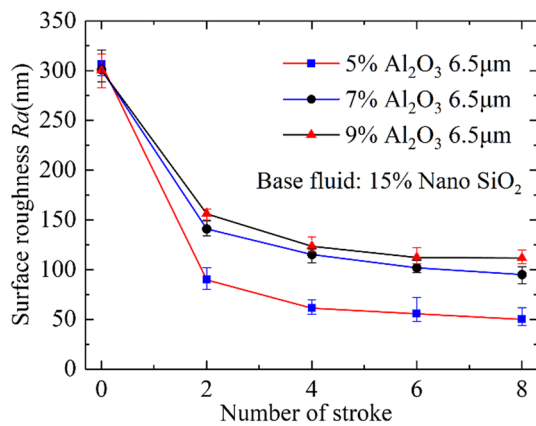


Fig. 7 Surface roughness variations versus grinding strokes at different abrasive mass fractions

the physical status of the developed abrasive system under different abrasive mass fractions. It was seen that the developed abrasive system became concentrated with the increase of the mass fractions of abrasive particles. The abrasive system with 5% abrasive mass fraction exhibited excellent flow characteristics. The nano-particle cluster effects easily occurred during high-shear and low-pressure grinding. The asperities on the workpiece surface was able to be rapidly removed. However, the shear-thickening property of the developed abrasive systems were gradually worsened with the increase of the abrasives mass fraction. The material removal capability from the workpiece surface asperities decreased accordingly during high-shear and low-pressure grinding. This resulted in poor surface roughness with the increase of the abrasive mass fraction.

It was found that the surface roughness rapidly decreased in the first 2–4 grinding strokes, as shown in Figs. 5, 6, and 7. Thereafter, the surface roughness varied slightly after 4 grinding strokes. This indicated that the rough surface is relatively easy to generate cluster effects. With the removal of the large asperities, the material removal on the smooth surface became relatively slow and stable. It was determined

that the optimal composition parameters of abrasive layer were 5% abrasive layer base fluid mass fraction, 7.0 μm abrasive grain size and 5% abrasive mass fraction.

3.3 Material Removal Depth

To investigate the influences of abrasive layer composition on the grinding performance, the material removal depth was analyzed and discussed. The weighing method was employed to obtain changes in workpiece weight at different grinding durations. The material removal depth was calculated accordingly. The accuracy of precision balance for weighing was 0.0001 g. The workpiece was ultrasonically cleaned with alcohol and dried with compress air to reduce weighing errors prior to weighing of each specimen.

3.3.1 Influence of Mass Fractions of Abrasive Layer Base Fluid on Material Removal Depth

Figure 9 shows the material removal depth versus grinding time at different mass fractions of abrasive layer base fluid when 5% abrasive mass fraction and 6.5 μm abrasive particle size was employed. After 8 grinding strokes (4 min), the material removal depths were 0.48 μm, 0.86 μm and 1.57 μm at 5%, 10% and 15% mass fraction of the base liquid, respectively. It was found that the material removal depth was largest when the mass fraction of the abrasive layer base liquid was selected as 15%. Meanwhile, the surface roughness of the workpiece was lowest (best). As explained, this was because the 15% mass fraction of the base liquid of the abrasive layer greatly enhanced the shear thickening properties of the abrasive system, which increased the number of abrasive particles in the cluster effects.

3.3.2 Influences of Average Abrasive Grain Size on Material Removal Depth

Figure 10 shows the variations of material removal depth versus grinding time at different average abrasive grain

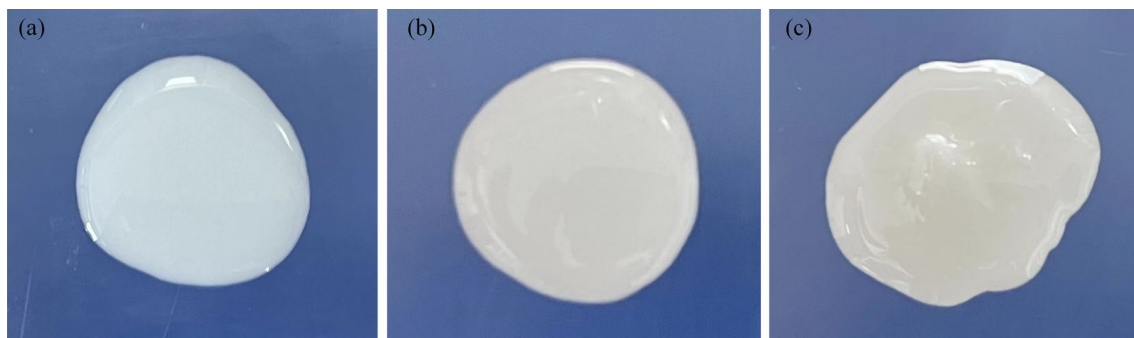


Fig. 8 The physical status of the developed abrasive system under different abrasive mass fractions of **a** 5%, **b** 7% and **c** 9%

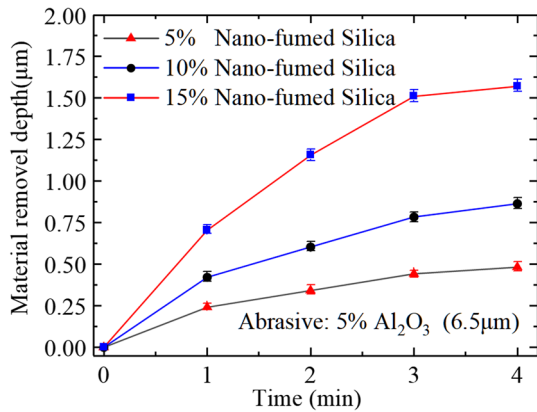


Fig. 9 Material removal depth variation versus grinding time at different mass fractions of abrasive layer base fluid

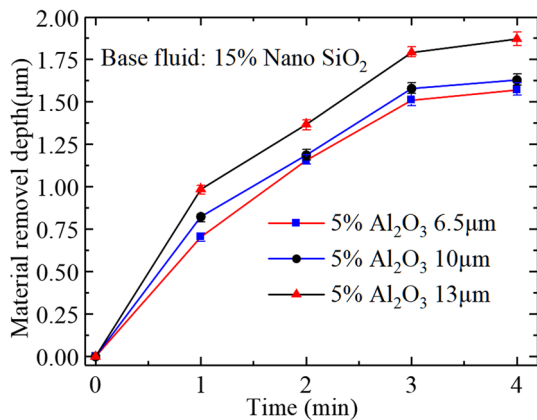


Fig. 10 Material removal depth variations versus grinding time at different average abrasive grain sizes

sizes when 5% abrasive mass fraction and 15% mass fraction of abrasive layer base liquid was selected. The material removal depths were 1.57 μm , 1.63 μm and 1.87 μm , at abrasive particle size of 6.5 μm , 10 μm and 13 μm , respectively. It was seen that the material removal depth was the largest at the average abrasive particle size of 13 μm . The material removal depth was proportional to the abrasive particle size. The amount of material removal increased with the increase of the abrasive size. The material removal depth was approximately 1.57 μm . However, the deep grinding scratches/textures worsen the ground surface quality. Meanwhile, it was seen that the trend of material removal depth versus grinding time was consistent at different abrasive grain sizes. The increasing ratio of material removal depth was large in the first 1–2 min grinding (2–4 grinding strokes). After grinding for ~ 2 min (~ 4 grinding strokes), the increasing ratio of the material removal depth gradually slowed down. The material removal capability decreased when the workpiece surface

became smooth during high-shear and low-pressure grinding.

3.3.3 Influences of Abrasive Mass Fractions on Material Removal Depth

Figure 11 shows the variations of material removal depth versus grinding time at different abrasive mass fractions. Material removal depth of 1.57 μm , 1.31 μm , and 0.79 μm were attained after 4 min of grinding with the abrasive mass fraction of 5%, 7%, and 9%, respectively. The maximum material removal depth was determined when the abrasive mass fraction was 5%, followed by 7% and 9%. The material removal depth was worst at the abrasive mass fraction of 9%. The trend of the material removal depth was the similar to the surface roughness. It was found that the surface quality was the worst at the abrasive mass fraction of 9%. As mentioned, the abrasive system with 5% abrasive mass fraction exhibited excellent flow characteristics. The nanoparticle cluster effects easily occurred during high-shear and low-pressure grinding. The shear-thickening property of the developed abrasive systems were gradually worsened with the increase of the abrasives mass fraction.

3.4 Surface Topography

3.4.1 Surface Morphologies at Different Grinding Strokes

Figure 12 shows the surface morphology of ground Inconel718 specimens at different grinding strokes. It can be seen that there are obvious surface defects such as scratches and pits on the initial specimen surface, as shown in Fig. 12a. After 2 grinding strokes, the initial shallow scratches and pits disappeared. A few of deep scratches remained, as shown in Fig. 12b. After 4 grinding strokes, several deep scratches and pits on the surface became shallow. The

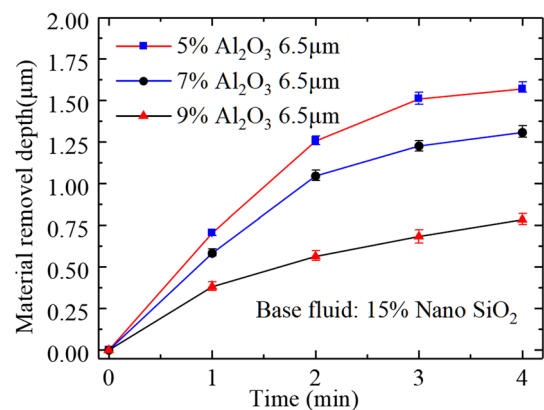


Fig. 11 Material removal depth variations versus grinding time at different abrasive mass fractions

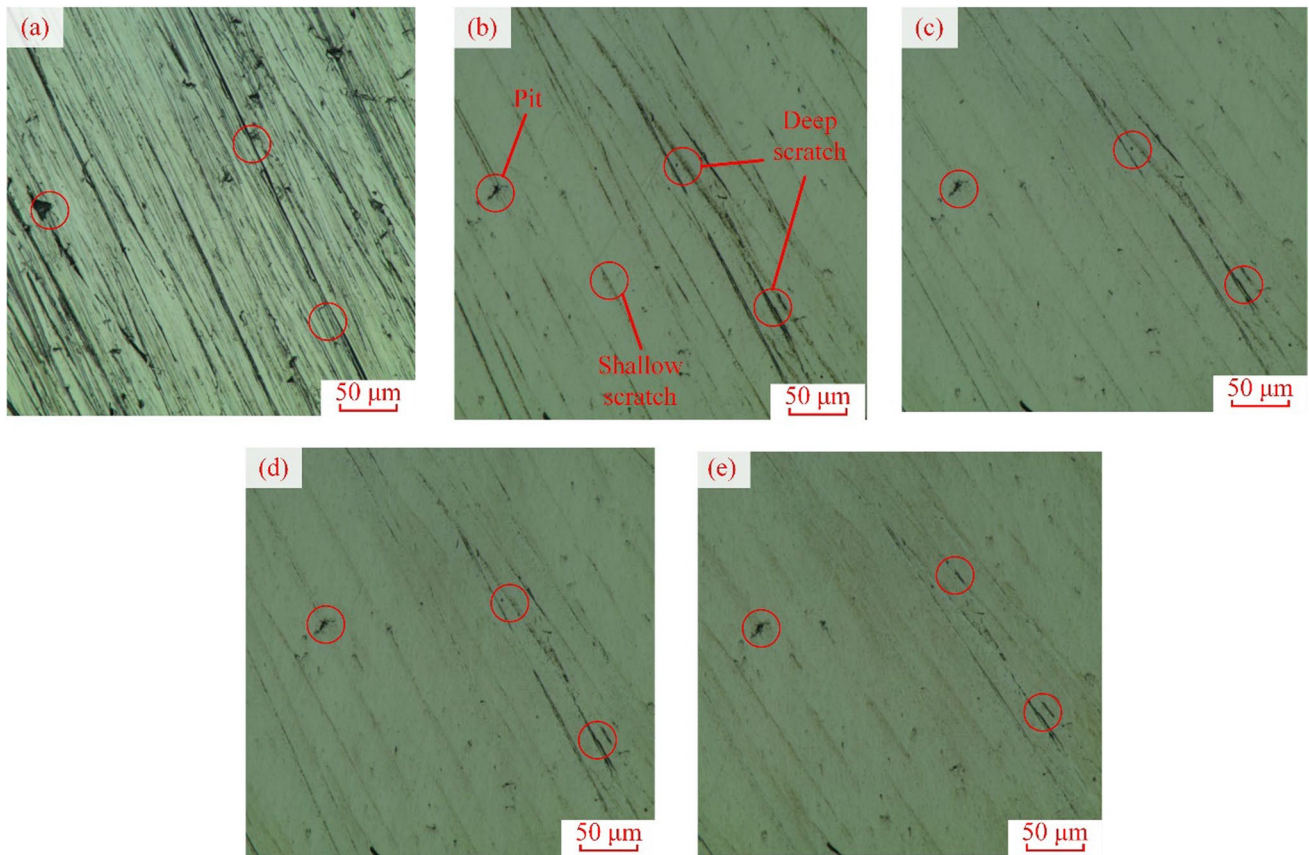


Fig. 12 Surface morphology at different grinding strokes: **a** 0 stroke, **b** 2 strokes, **c** 4 strokes, **d** 6 strokes, and **e** 8 strokes

ground surface became smooth. As shown in Figs. 12d and e, it can be identified that the residual scratches and pits on the specimen surface gradually become shallow after 6–8 grinding strokes. The surface quality was greatly improved. Few shallow residual scratches remained.

Moreover, the SEM images of specimens before and after grinding were observed and analyzed. As shown in Fig. 13, the original scratches were almost removed after high-shear and low-pressure grinding. The grinding texture is uniformly generated on the workpiece surface. There were several residual deep scratches after 8 grinding strokes.

3.4.2 Three-Dimensional Morphology at Different Grinding Strokes

Figure 14 shows the three-dimensional topography of Inconel718 specimens examined at different grinding strokes to explore the surface topography evolution. The objective lens magnification was chosen as $\times 10$. It was determined that the surface roughness (Sa) decreased as the grinding stroke increased. It was consistent with the variation of the surface roughness (Ra). It demonstrated that surface quality was improved with the increase of the grinding strokes.

Figure 15 exhibits the variation of surface profile curve of the specimen at different grinding strokes. It was observed that the workpiece surface gradually became smooth while excellent profile accuracy was maintained after 8 grinding strokes.

3.5 Grinding Force with Pure Fiber and Abrasive Layer

Figure 16 shows the comparison of grinding force with the pure fiber and abrasive layer. It was seen that the normal grinding force slightly decreased in the first ~ 2 s and then increased slowly as the abrasive tool came into contact with the specimen surface. This was caused by the super elastic properties of the rubber material in the ECAT. The stable grinding stage was obtained during the period of full contact of the ECAT with the specimen surface.

Figure 17 shows grinding force examined at 0.1 s. The average ratio of tangential force (F_t) to normal force (F_n) of the abrasive layer with the abrasive system was 0.2741. It was much larger than that of pure fabrics without the abrasive system i.e. 0.1560. The high-shear and low-pressure grinding with ECAT was therefore validated with the large

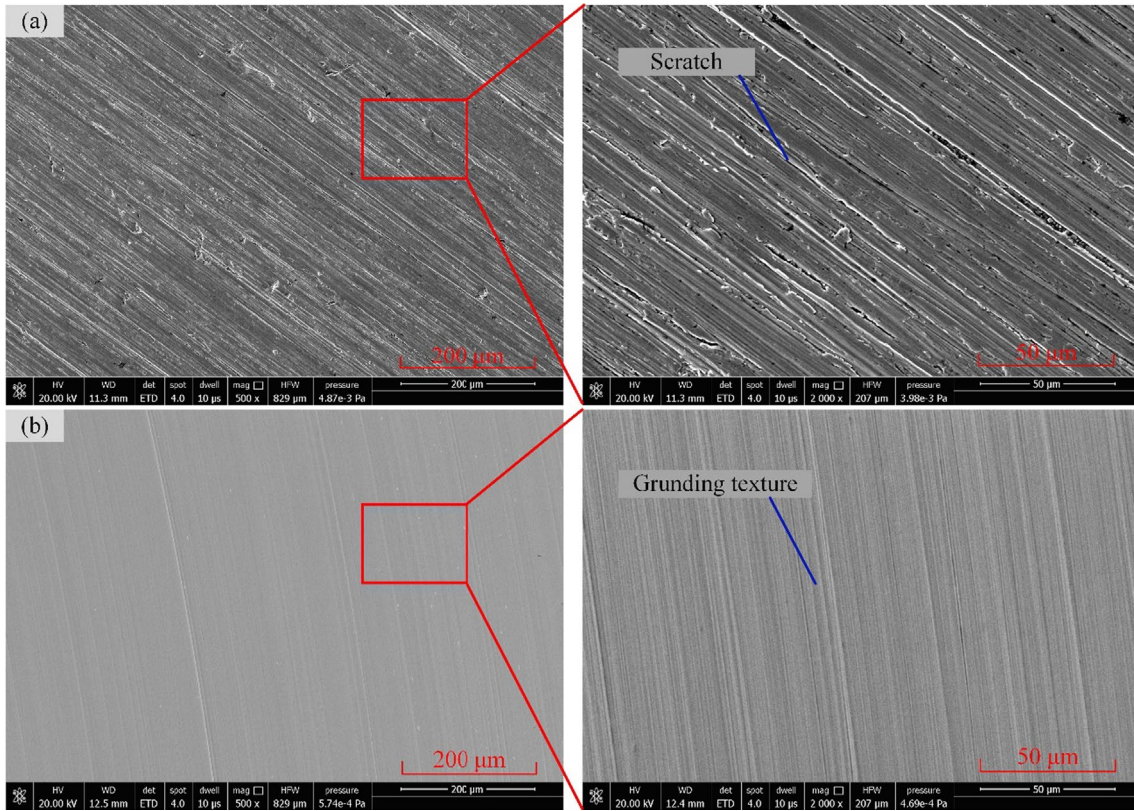


Fig. 13 Grinding texture of Inconel718 alloy specimen: **a** before and **b** after grinding

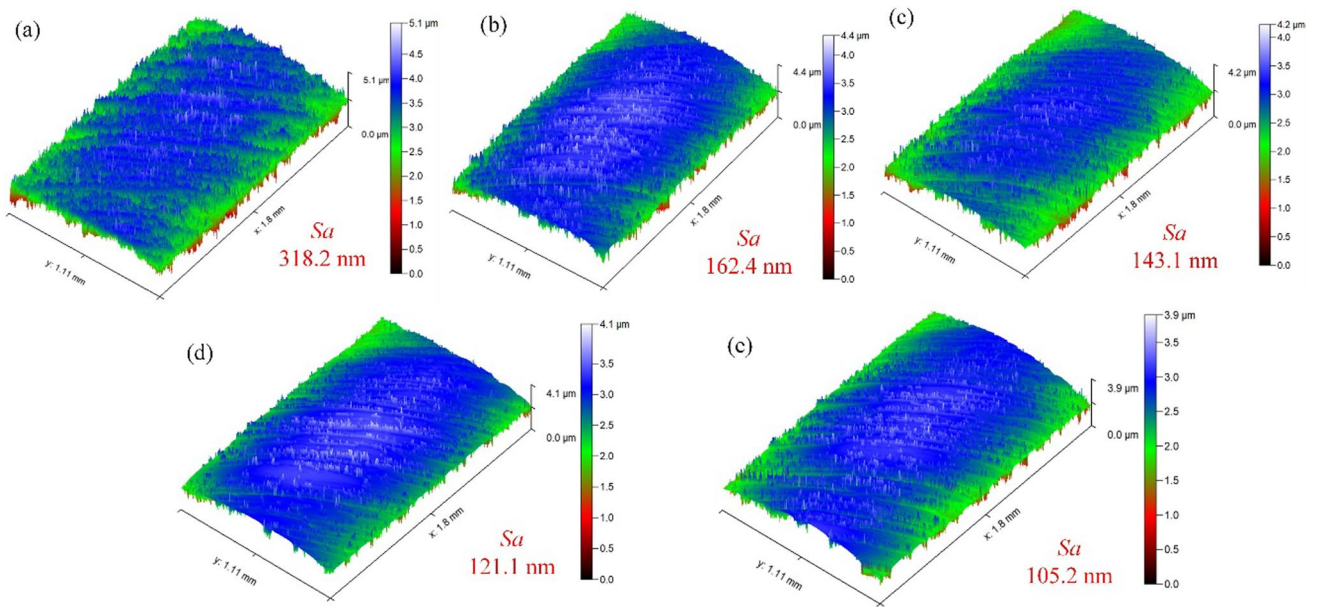


Fig. 14 Three-dimensional morphologies at different strokes: **a** 0 stroke, **b** 2 stroke, **c** 4 stroke, **d** 6 stroke, **e** 8 stroke

average force ratio of tangential to normal force. During high-shear and low-pressure grinding, the ECAT contacts with the micro-convex peaks on the workpiece surface at

high speed. Particle clusters occur in the abrasive layer of the ECAT that acts on micro-convex peaks under the cluster effects [26]. The tangential force significantly increases

Fig. 15 Surface profile curves of Inconel718 alloy specimen at different grinding strokes

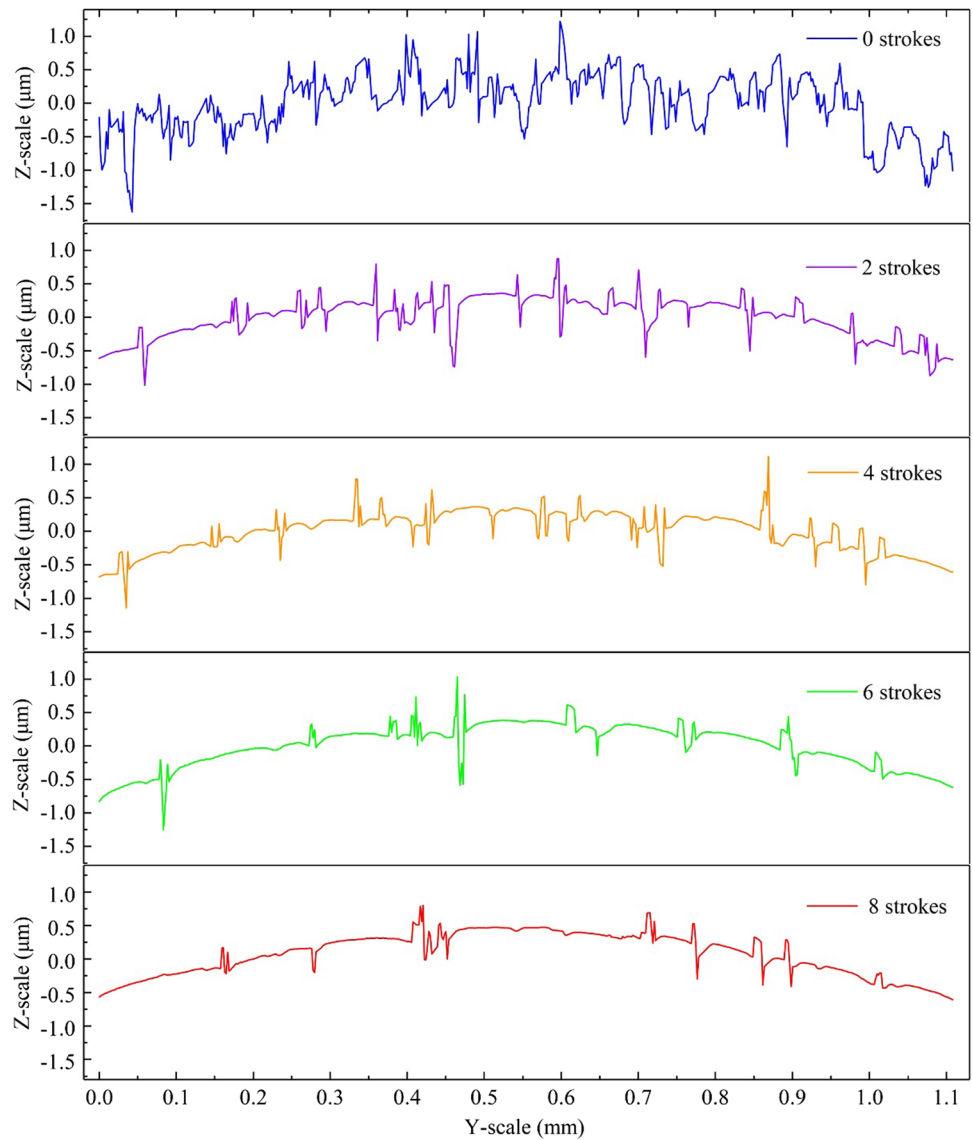
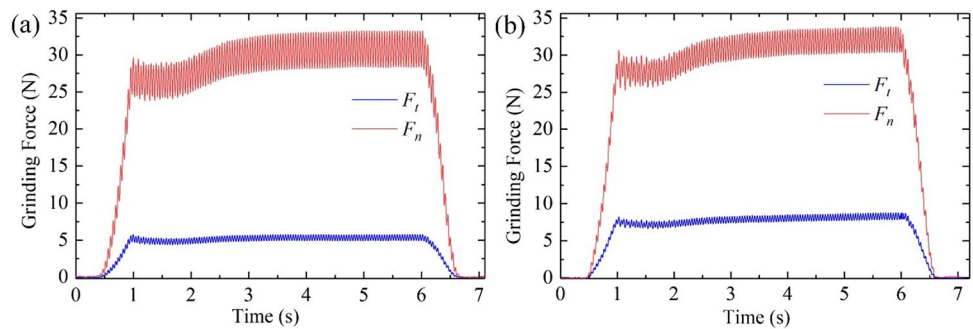


Fig. 16 Grinding process force comparison with pure fiber and abrasive layers



while the normal decreases during ECAT grinding [26]. Thereby, the asperities on the workpiece surface are removed under the high-shear and low-pressure regime.

Figure 18 exhibits the curved Inconel718 specimens before and after grinding. It can be seen that ultra-smooth curved surface was attained after grinding.

Fig. 17 Grinding force curves with pure fiber and abrasive layer

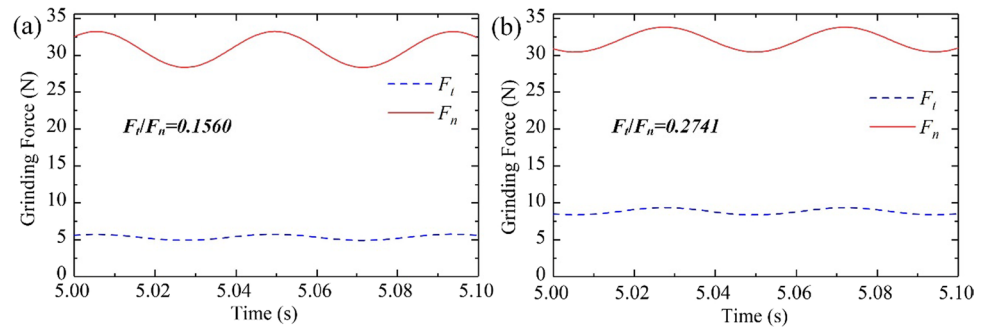
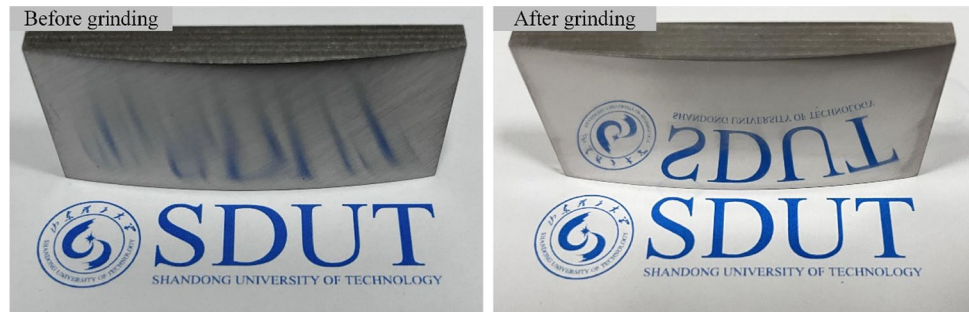


Fig. 18 Comparison of curved Inconel718 specimens before and after grinding



4 Conclusions

In this study, the high-shear and low-pressure grinding method for curved parts was proposed with the developed super-elastic composite abrasive tool (ECAT). Grinding experiments were carried out on curved Inconel718 specimens. The main conclusions were obtained as follows.

- (1) The influence of different abrasive layer composition parameters on surface roughness was studied. The optimal composition parameters of the abrasive layer are the abrasive layer base fluid mass fractions of 5%, abrasive grain size of $6.5\ \mu\text{m}$ and the abrasive mass fraction of 5%. Under the optimal condition of parameter, the surface roughness decreased from 306.4 to 50.0 nm after 8 grinding strokes. The excellent grinding performance was verified using the developed ECAT.
- (2) The influence of different abrasive layer composition parameters on material removal depth was examined. The ECAT demonstrated excellent material removal capability. The material removal depth was approximately $1.57\ \mu\text{m}$ under the optimal conditions.
- (3) The surface morphology, SEM and surface profile of the specimen under different grinding strokes were observed. The initial scratches, pits and other surface defects on workpiece were almost removed after 8 grinding strokes. The fine grinding textures were formed while excellent profile accuracy was maintained using the developed ECAT.

- (4) The average ratio of tangential to normal force with the abrasive system in the ECAT was larger than that of the pure fabrics without the abrasive system. The high-shear and low-pressure grinding characteristic was verified for the curved parts made of the Inconel718 materials.

Acknowledgements This research was funded by the National Natural Science Foundation of China (51875329), Shandong Provincial Natural Science Foundation, China (Grant No. ZR2023ME112), Taishan Scholar Foundation of Shandong Province (tsqn201812064), Innovation Capacity Improvement Program for High-tech SMEs of Shandong Province (2022TSGC1333, 2022TSGC1261), and Scientific Innovation Project for Young Scientists in Shandong Provincial Universities (2019KJB030).

References

1. Bartolomeis, A. D., Newman, S. T., Jawahir, I. S., Biermann, D., & Shokrani, A. (2021). Future research directions in the machining of Inconel718. *Journal of Materials Processing Technology*, 297, 117260. <https://doi.org/10.1016/j.jmatprotec.2021.117260>
2. Li, Y. H., Zhang, Z., & Guan, Y. C. (2020). Thermodynamics analysis and rapid solidification of laser polished Inconel718 by selective laser melting. *Applied Surface Science*, 511, 145423.1-145423.7. <https://doi.org/10.1016/j.apsusc.2020.145423>
3. Wang, B. K., Ji, R. J., Gong, Z., Zhao, Q. Y., Liu, Y. H., Jin, H., Wang, L. X., Xu, Z. Q., Cai, B. P., & Ma, J. M. (2022). Effect of water in oil emulsion on the surface quality of Inconel 718 alloy during coupling electrical pulse and ultrasonic treatment. *Surface and Coatings Technology*, 437, 437128355. <https://doi.org/10.1016/j.surfcoat.2022.128355>

4. Shang, Z., Wei, X. P., Song, D. Z., Zou, J. Y., Liang, S. H., Liu, G., Nie, L. P., & Gong, X. F. (2020). Microstructure and mechanical properties of a new nickel-based single crystal superalloy. *Journal of Materials Research and Technology*, 9, 11641–11649. <https://doi.org/10.1016/j.jmrt.2020.08.032>
5. Zhu, D. H., Zhang, X. M., & Ding, H. (2013). Tool wear characteristics in machining of nickel-based superalloys. *International Journal of Machine Tools and Manufacture*, 64, 60–77. <https://doi.org/10.1016/j.ijmactools.2012.08.001>
6. Gao, W., Li, M. Q., Yin, H. P., Zhang, Y. X., & Liu, Z. H. (2023). Effect of dressing with form grinding wheel on grinding surface integrity of 18CrNiMo7-6 steel. *Diamond & Abrasives Engineering*, 43, 632–639. <https://doi.org/10.13394/j.cnki.jgszz.2022.0170>
7. Mukhopadhyay, M., Kundu, P. K., & Das, S. (2018). Experimental investigation on enhancing grindability using alkaline-based fluid for grinding Ti–6Al–4V. *Materials and Manufacturing Processes*, 33, 1775–1781. <https://doi.org/10.1080/10426914.2018.1476759>
8. Dong, G. J., & Zhang, L. M. (2019). Investigation on grinding force and machining quality during rotary ultrasonic grinding deep-small hole of fluorophlogopite ceramics. *The International Journal of Advanced Manufacturing Technology*, 104(1–4), 2815–2825. <https://doi.org/10.1007/s00170-019-04138-7>
9. Zhang, Y. B., Li, C. H., Ji, H. J., Yang, X. H., Yang, M., Jia, D. Z., Zhang, X. P., Li, R. Z., & Wang, J. (2017). Analysis of grinding mechanics and improved predictive force model based on material-removal and plastic-stacking mechanisms. *International Journal of Machine Tools and Manufacture*, 122, 81–97. <https://doi.org/10.1016/j.ijmactools.2017.06.002>
10. Sun, J. L., Qin, F., Chen, P., & An, T. (2016). A predictive model of grinding force in silicon wafer self-rotating grinding. *International Journal of Machine Tools and Manufacture*, 09, 74–86. <https://doi.org/10.1016/j.ijmactools.2016.07.009>
11. Tian, Y. B., Liu, F., Wang, Y., & Wu, H. (2017). Development of portable power monitoring system and grinding analytical tool. *Journal of Manufacturing Processes*, 27, 188–197. <https://doi.org/10.1016/j.jmappro.2017.05.002>
12. Hatami, O., Adibi, H., & Rezaei, M. S. (2022). Application of a compressed air jet for cleaning of wheel surface in grinding nickel-based super alloy Inconel 718. *CIRP Journal of Manufacturing Science and Technology*, 37, 233–244. <https://doi.org/10.1016/J.CIRPJ.2022.02.004>
13. Lerra, F., Candido, A., Liverani, E., & Fortunato, A. (2022). Prediction of micro-scale forces in dry grinding process through a FEM-ML hybrid approach. *International Journal of Precision Engineering and Manufacturing*, 23, 15–29. <https://doi.org/10.1007/s12541-021-00601-2>
14. Zhang, J. F., Shi, Y. Y., Lin, X. J., & Duan, J. H. (2017). Free-style belt polishing technology for leading and trailing edges of aero-engine blade. *Acta Aeronautica Astronautica Sinica*, 38(3), 420327. <https://doi.org/10.7527/S1000-6893.2016.0179>
15. Huang, X. K., Chai, Z., Cao, F., Ren, X. K., Chen, H. B., Wang, H., Lu, W. F., & Chen, X. Q. (2022). Isotropic etching polishing of belt ground Inconel 718 to improve surface strengthening and quality. *Surface and Coatings Technology*, 436, 128292. <https://doi.org/10.1016/j.surfcoat.2022.128292>
16. Wei, S. L., Zhang, T., Wei, H. J., Wang, W., Wang, H. Y., & Liu, Y. D. (2023). Simulation study on removal mechanism of Si₃N₄ ceramic in rotary ultrasonic grinding. *International Journal of Precision Engineering and Manufacturing*, 24, 945–965. <https://doi.org/10.1007/s12541-023-00808-5>
17. Song, J. F., & Yao, Y. X. (2015). Material removal model considering influence of curvature radius in bonnet polishing convex surface. *Chinese Journal of Mechanical Engineering*, 28(6), 1109–1116. <https://doi.org/10.3901/CJME.2015.0923.114>
18. Bingham, R. G., Walker, D. D., Kim, D-H., Brooks, D., Freeman, R., & Riley, D. (2000). Novel automated process for aspheric surfaces. In *International Society Optical Engineering*, 4093, 445–450. <https://doi.org/10.1117/12.405237>
19. Beaucamp, A., Namba, Y., Combrinck, H., Charlton, P., & Freeman, R. (2014). Shape adaptive grinding of CVD silicon carbide. *CIRP Annals*, 63(1), 317–320. <https://doi.org/10.1016/j.cirp.2014.03.019>
20. Cao, Z. C., Cheung, C. F., Ho, L. T., & Liu, M. Y. (2017). Theoretical and experimental investigation of surface generation in swing process bonnet polishing of complex three-dimensional structured surfaces. *Precision Engineering*, 50, 361–371. <https://doi.org/10.1016/j.precisioneng.2017.06.010>
21. Zhu, Z. Q., Chen, Z. T., & Zhang, Y. (2021). A novel polishing technology for leading and trailing edges of aero-engine blade. *The International Journal of Advanced Manufacturing Technology*, 116, 1871–2188. <https://doi.org/10.1007/S00170-021-07574-6>
22. Zeng, X., Ji, S. M., Tan, D. P., Jin, M. S., Wen, D. H., & Zhang, L. (2013). Softness consolidation abrasives material removal characteristic oriented to laser hardening surface. *The International Journal of Advanced Manufacturing Technology*, 69(9–12), 2323–2332. <https://doi.org/10.1007/s00170-013-4985-y>
23. Wang, S., Zhao, Q. L., & Guo, B. (2023). Ultra-precision ductile grinding of off-axis biconical free-form optics with a controllable scallop height based on slow tool servo with diamond grinding wheels. *International Journal of Precision Engineering and Manufacturing-Green Technology*, 10, 1169–1188. <https://doi.org/10.1007/s40684-022-00481-5>
24. Li, M., Lyu, B. H., Yuan, J. L., Dong, C. C., & Dai, W. T. (2015). Shear-thickening polishing method. *International Journal of Machine Tools and Manufacture*, 94, 88–99. <https://doi.org/10.1016/j.ijmactools.2015.04.010>
25. Shao, Q., Lyu, B. H., Yuan, J. L., Wang, X., Ke, M. F., & Zhao, P. (2021). Shear thickening polishing of the concave surface of high-temperature nickel-based alloy turbine blade. *Journal of Materials Research and Technology*, 11, 72–84. <https://doi.org/10.1016/J.JMRT.2020.12.112>
26. Tian, Y. B., Li, L. G., Fan, S., Guo, Q. J., & Cheng, X. (2021). A novel high-shear and low-pressure grinding method using specially developed abrasive tools. *Proceedings of the Institution of Mechanical Engineers, Part B: Journal of Engineering Manufacture*, 235(1–2), 166–172. <https://doi.org/10.1177/0954405420949106>
27. Tian, Y. B., Li, L. G., Liu, B., Han, J. G., & Fan, Z. H. (2020). Experimental investigation on high-shear and low-pressure grinding process for Inconel718 superalloy. *The International Journal of Advanced Manufacturing Technology*, 107(7–8), 3425–3435. <https://doi.org/10.1007/s00170-020-05284-z>
28. Wang, Z. K., Yang, Y. K., Zhang, Z., Pang, M. H., Liang, M. C., Ma, L. J., & Su, J. X. (2023). A novel technique for dressing fixed abrasive lapping pad with abrasive water jet. *International Journal of Precision Engineering and Manufacturing*, 10, 1351–1373. <https://doi.org/10.1007/s40684-022-00500-5>
29. Gu, Z. Q., Tian, Y. B., Han, J. G., Wei, C. W., Babbar, A., & Liu, B. (2022). Characteristics of high-shear and low-pressure grinding for Inconel718 alloy with a novel super elastic composite abrasive tool. *The International Journal of Advanced Manufacturing Technology*, 123, 345–355. <https://doi.org/10.1007/s00170-022-10179-2>
30. Tian, C. J., Han, J. G., Tian, Y. B., Liu, B., Gu, Z. Q., & Hu, X. T. (2021). Simulation analysis of cluster effect of high-shear low-pressure grinding with flexible abrasive tools. *Micromachines*, 12(7), 827. <https://doi.org/10.3390/M12070827>
31. Yoon, J. S., Kim, Y. D., Lee, J., & Lee, D. Y. (2023). OPC UA-based machining cell monitoring system for multi-vendors'

machine tools and industrial robots. *International Journal of Precision Engineering and Manufacturing*, 1, 63–69. <https://doi.org/10.57062/ijpem-st.2022.0024>

Publisher's Note Springer Nature remains neutral with regard to jurisdictional claims in published maps and institutional affiliations.

Springer Nature or its licensor (e.g. a society or other partner) holds exclusive rights to this article under a publishing agreement with the author(s) or other rightsholder(s); author self-archiving of the accepted manuscript version of this article is solely governed by the terms of such publishing agreement and applicable law.



Yebing Tian was born in Jining, China in 1979. He is currently a full professor in School of Mechanical Engineering, Shandong University of Technology, China. He received his Ph. D from Dalian University of Technology, China in 2007. His research interests include ultra-precision grinding, polishing and intelligent monitoring.



Zhiqiang Gu was born in Laiwu, China in 1998. He received his M. E. degree from School of Mechanical Engineering, Shandong University of Technology, China. His research interest is ultra-precision grinding.



Sohini Chowdhury was born in Sunabeda, India in 1991. She received her Ph. D from North Eastern Regional Institute of Science and Technology, India, in 2020. Her research interest is ultra-precision grinding.



Jinguo Han was born in Linyi, China in 1989. He is currently a associate professor in School of Mechanical Engineering, Shandong University of Technology, China. He received his Ph. D from Changchun University of Technology, China, in 2018. His research interests include ultra-precision cutting and ultrasonic-assisted machining.



Chengwei Wei was born in Liaocheng, China in 1999. He is currently a Ph. D student in School of Mechanical Engineering, Shandong University of Technology, China. His research interest is ultra-precision grinding.



Xinyu Fan was born in Weifang, China in 2000. He is currently a M.E. student in School of Mechanical Engineering, Shandong University of Technology, China. His research interest is ultra-precision grinding.